

PAPER • OPEN ACCESS

Overview of damage to beryllium limiters by unmitigated disruptions and runaway electrons in the JET tokamak with metal walls

To cite this article: I. Jezu *et al* 2024 *Nucl. Fusion* **64** 106047

View the [article online](#) for updates and enhancements.

You may also like

- [Physics basis for the divertor tokamak test facility](#)
F. Crisanti, R. Ambrosino, M.V. Falessi et al.
- [Density profiles in stellarators: an overview of particle transport, fuelling and profile shaping studies at TJ-II](#)
J.A. Alonso, D. Alegre, J. Alonso et al.
- [The core–edge integrated neon-seeded scenario in deuterium–tritium at JET](#)
C. Giroud, I.S. Carvalho, S. Brezinsek et al.

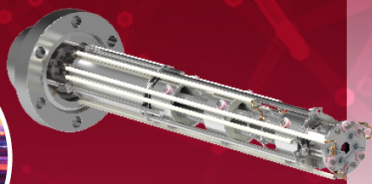
Mass spectrometers for vacuum, gas, plasma and surface science

HIDEN
ANALYTICAL

Ultra-high Resolution Mass Spectrometers for the Study of Hydrogen Isotopes and Applications in Nuclear Fusion Research

DLS Series

- ▶ **Unique** Dual Mass range / Zone H functionality
- ▶ For the measurement of overlapping species
- ▶ He/D2, CH2D2/H2O, Ne/D2O



HAL 101X

- ▶ Monitoring, diagnostics and analysis applications in tokamak and torus operations
- ▶ Unique design avoids all radiation shielding requirements
- ▶ Featuring TIMS mode for real-time quantification of hydrogen and helium isotopes



Overview of damage to beryllium limiters by unmitigated disruptions and runaway electrons in the JET tokamak with metal walls

I. Jepu^{1,*} , A. Widdowson¹ , G.F. Matthews¹, J.P. Coad¹, J. Likonen², S. Brezinsek^{3,4} , M. Rubel⁵ , G. Pintsuk³ , P. Petersson⁵, E. Fortuna-Zalesna⁶ , J. Grzonka⁶, C. Porosnicu⁷ , P. Dinca⁷ , O. Pompilian⁷ , B. Butoi⁷ , S. G. Moga⁸ , S. Silburn¹ , S. Kuksenko¹ , E. Alves⁹ , N. Catarino⁹ , R.A. Pitts¹⁰ , L. Chen¹⁰ , S. Ratynskaia¹¹ 
and JET Contributors^a

¹ UKAEA (United Kingdom Atomic Energy Authority), Culham Campus, Abingdon, Oxfordshire, United Kingdom of Great Britain and Northern Ireland

² VTT Technical Research Centre of Finland, VTT, Espoo, Finland

³ Forschungszentrum Juelich GmbH, EURATOM Association, Juelich, Germany

⁴ Heinrich-Heine-Universität Düsseldorf, Mathematisch-Naturwissenschaftliche Fakultät, Düsseldorf 40225, Germany

⁵ Division of Electromagnetism and Fusion Science, KTH Royal Institute of Technology, Stockholm, Sweden

⁶ Faculty of Materials Science and Engineering, Warsaw University of Technology, Warsaw, Poland

⁷ National Institute for Laser Plasma and Radiation Physics, Bucharest-Magurele, Romania

⁸ Natl Univ Sci & Technol POLITEHN Bucharest, Reg Ctr Res & Dev Mat, Proc & Innovat Prod Dedicated Automot Ind CRCD AUT, Pitesti Univ Ctr, Pitesti, Romania

⁹ IPFN, Instituto Superior Técnico, Universidade de Lisboa, Lisboa, Portugal

¹⁰ ITER Organization, St-Paul-lez-Durance Cedex, France

¹¹ Space and Plasma Physics, KTH Royal Institute of Technology, Stockholm, Sweden

E-mail: ionut.jepu@ukaea.uk

Received 19 January 2024, revised 29 May 2024

Accepted for publication 22 July 2024

Published 11 September 2024



Abstract

The Joint European Torus (JET) fusion reactor was upgraded to the metallic wall configuration in 2011 which consisted of bulk beryllium (Be) tiles in the main chamber and bulk tungsten (W) and W-coated CFC tiles in the divertor (Matthews G.F. *et al* 2011 *Phys. Scr.* **T148** 014001). During each campaign, a series of wall damages were observed; on the upper dump plates (UDP) positioned to the top part of the vessel walls and on the inner wall—mainly affecting the inner wall guard limiters (IWGL). In both cases, it was concluded that the causes of these damages were unmitigated plasma disruptions. In the case of JET with the metallic wall configuration, most of these plasma disruptions were intentionally provoked. The overall objective was to study the behaviour of these phenomena, in order to assess their impact on the wall, improve understanding of morphological material changes, and—based on that—to

^a See Maggi *et al* 2024 (<https://doi.org/10.1088/1741-4326/ad3e16>) for JET Contributors.

* Author to whom any correspondence should be addressed.



Original content from this work may be used under the terms of the [Creative Commons Attribution 4.0 licence](https://creativecommons.org/licenses/by/4.0/). Any further distribution of this work must maintain attribution to the author(s) and the title of the work, journal citation and DOI.

develop, implement and test mitigation techniques for their prospective use on ITER. The current results bring additional information on the effects of the unmitigated plasma disruptions on the UDPs and are a significant extension of work presented in (Jezu *et al* 2019 *Nucl. Fusion* 59 086009) where the scale of the damage after three operational campaigns on the Be top limiters of JET was highlighted. In addition, new data is presented on the damaging effect that the high energetic runaway electrons had on the Be IWGL in JET.

Keywords: JET, beryllium, plasma disruptions, runaway electrons, material damage

(Some figures may appear in colour only in the online journal)

1. Introduction

Future generation tokamaks, including ITER, will strive for better confinement, which means a higher plasma current, I_p to achieve high fusion gain [1]. One of the major issues when operating at high I_p is a potential for increased damage of first wall components due to unmitigated plasma disruptions and production of Runaway Electrons (RE). Two direct consequences of disruptions and REs are: (i) high thermal loads with fast melting and melt motion due to electromagnetic forces, as previously seen in Joint European Torus (JET) [2] and TEXTOR [3] and (ii) localised melting from RE impact as reported in JET [4]. Aside from the damage to plasma-facing components (PFC), the production of droplets arising from melting may act as a dust source. This paper delivers, an overview of the melt damage to beryllium (Be) first wall components as a direct consequence of unmitigated plasma disruptions and REs on the former called JET ITER-Like Wall [5] is presented. Such Be components provide a unique source of material for characterising the impact of melt damage on components and for benchmarking melt damage modelling in ITER.

The damage caused by disruptions and REs result in distinct morphological and structural changes. These modifications can be directly correlated based on data collection during and shortly after the damaging events, using near-infrared camera imaging and thermocouple measurements. In addition, following sessions causing damage, in-vessel inspection was possible without the need to breach the vacuum, so there was a well-known audit of damage to components. The type of damage was also correlated with the experimental aims of different campaign periods. In the first ITER Like Wall (ILW-1) campaign from 2011–2012, the focus was on the impact of the new wall on plasma operations during which $\sim 11\%$ of the pulses ended with unmitigated disruptions. In most of the cases, they were not heavily affecting the main chamber wall components. The second campaign (2013–2014) (ILW-2) was dedicated to high power scenarios and integration of necessary tools for disruption mitigations. During this period disruptions and REs were intentionally generated in dedicated sessions. In total, after three ILW campaigns (2011–2016) $\sim 15\%$ of the pulses were catalogued as disruptions, but in essence just a few were heavily damaging the main chamber PFCs, and the majority of these happened during the second campaign. Each operational campaign was followed by an intervention when, in addition to maintenance activities, components were removed/replaced

for post-mortem analysis. The current work combines new findings on layer melting, molten material movement and material loss from the upper dump plates (UDP), a continuation of the findings presented in [2] discussing the first damage type (i), along with novel data on the damage caused by the RE impacts on the Be inner wall limiters (IWGL) contributing to the second damage scenario (ii). New data are presented through various methods including imaging analysis and near infra-red camera imaging in vessel, and post-mortem accurate weight measurements, surface profiling, and evaluations of morphology and structure.

2. Beryllium melting under high heat loads in unmitigated disruptions (i)

Results presented in [2] highlighted melting and erosion of the UDPs in JET reactor during the first three experimental campaigns (I: 2011–2012; II: 2013–2014; III: 2015–2016) with a metallic wall configuration. Each UDP is a poloidal beam of eight Be tiles attached to the top of the vacuum vessel, numbered DP1 (inboard) to DP8 (outboard), as shown in figure 1. There are 64 UDP beams toroidally. The main reason for the Be melting phenomena on the upper part of the reactor was identified as being the unmitigated plasma disruptions. The migration of the Be layer along the tile surface during the thermal and current quench phases of unmitigated upward going vertical displacement events was caused by the $\mathbf{j} \times \mathbf{B}$ forces acting on the molten surface, as evidenced by the damages induced on the UDP beam of tiles and described in [2]. Due to the melt layer motion in the poloidal direction, bridging between neighbouring castellation was observed and documented for the first time. Be layer movement in the poloidal direction was previously documented in JET for the inner and outer limiter tiles (IWGL and OPL) [6, 7] and also observed for W melting and layer propagation in TEXTOR reactor [3]. In the case of all 64 DP8 tiles, it was shown that the $\mathbf{j} \times \mathbf{B}$ force generates Be structures like an inversed ‘waterfall’ which are discussed in section 2.1. It was highlighted that the electromagnetic forces acting on the melt layer also caused the ejection of droplets from the tip of the Be ‘waterfall’ structures onto the vessel walls in the proximity of the DP8. Extensive modelling using MEMOS-U and two-dimensional ANSYS Fluent Navier–Stokes simulation codes confirmed the experimental observations in [2] in terms of melt layer dynamics along the tile [8] and material ejection from the UDP [9].

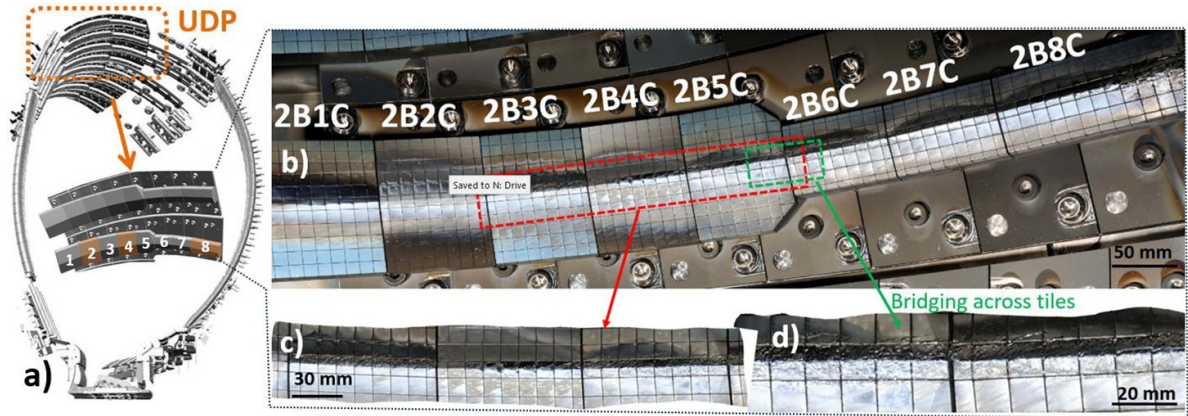


Figure 1. Cross section of JET vessel with a focus on the UDP sector (a) with in-vessel images of 2BC dump plate beam (b) which was partially removed (DP1 to DP5) for weighing exercise during intervention after second and third ILW campaigns, and close-up image (c) and (d) showing Be layer movement across DP3 and DP6.

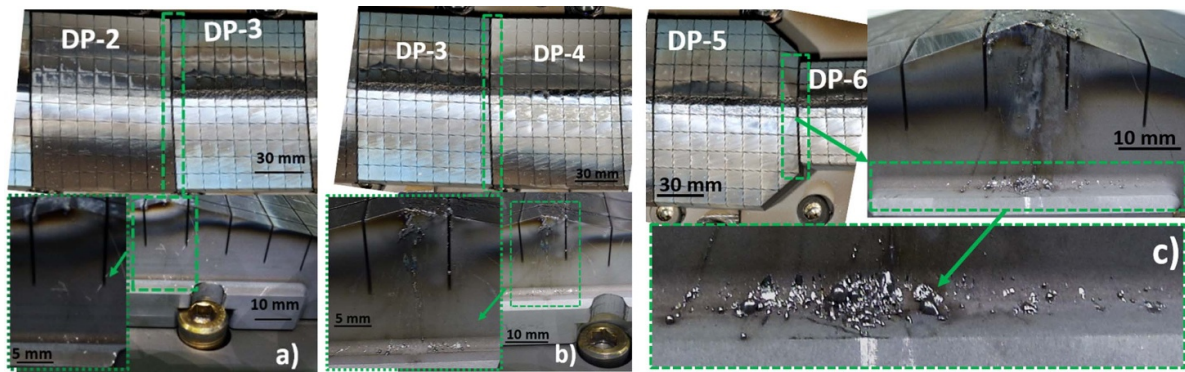


Figure 2. Photographs of dump plate tiles with close-up views showing beryllium droplets found in the gaps between tiles. (a) DP2 and DP3; (b) DP3 and DP4 and (c) DP5 and DP6 where most Be droplets were found.

2.1. Melt layer movement and material loss

An additional photographic survey was conducted on the entire beam of tiles of the UDPs. The results of the survey show new evidence that molten material can travel sufficient distances to potentially create bridges between adjacent tiles. Figure 1(a) highlights the cross section of JET vessel with the focus on the UDP sector. Detailed evidence of Be melt layer movement and castellation bridging is highlighted in figures 1(b)–(d) for tiles DP3 to DP6. One can observe an enhancement of the melt layer movement, towards the low field side generated by the $\mathbf{j} \times \mathbf{B}$ forces in the poloidal direction. Tile bridging is also observed towards the low field side. However, due to the larger gaps between tiles, some Be droplets were found in between the tiles. Small amounts of Be droplets can be seen on the DP2 tile, they are shown in figure 2(a). The amount of Be discovered in the form of droplets is reduced relative to the other tiles because this tile is replaced with a brand new one following each operational campaign in the metallic wall configuration. Therefore, the damage on it results from a single campaign, not from all three. More droplets are evident between tiles DP3 and DP4 in figure 2(b), and even more between tiles DP5 and DP6,

as shown in figure 2(c). In both locations, many Be droplets of various sizes can be seen in the spaces clearly indicating that layer migration occurs. In addition, bridging across castellation previously reported within a single tile, is also observed across neighbouring tiles despite the larger gaps. A significant number of resolidified beryllium droplets has been found in gaps between DP tiles towards the low field side. This shows that long range pathways for the gradual migration of melted material from the high field side to the low field side of the UDP beam is possible although some evidence of bridging between tiles may have been lost during the tile removal actions necessary during inter-campaign interventions. It is quite likely that molten Be material migrates from one tile to another once a bridge between tiles is built, but only if the gap between tiles is not too large to prevent such bridging. Based on the current imaging assessment it was shown that more melt in the form of resolidified droplets is found towards the low field side in the gaps of each tile. At this stage, there is no clear evidence that material mobilized from the high field side of the UDP beam, namely DP1, can travel as far as to the low field side, namely on the DP8. However, it is highly likely for this to happen in designs where gaps between tiles are smaller towards the low field side.

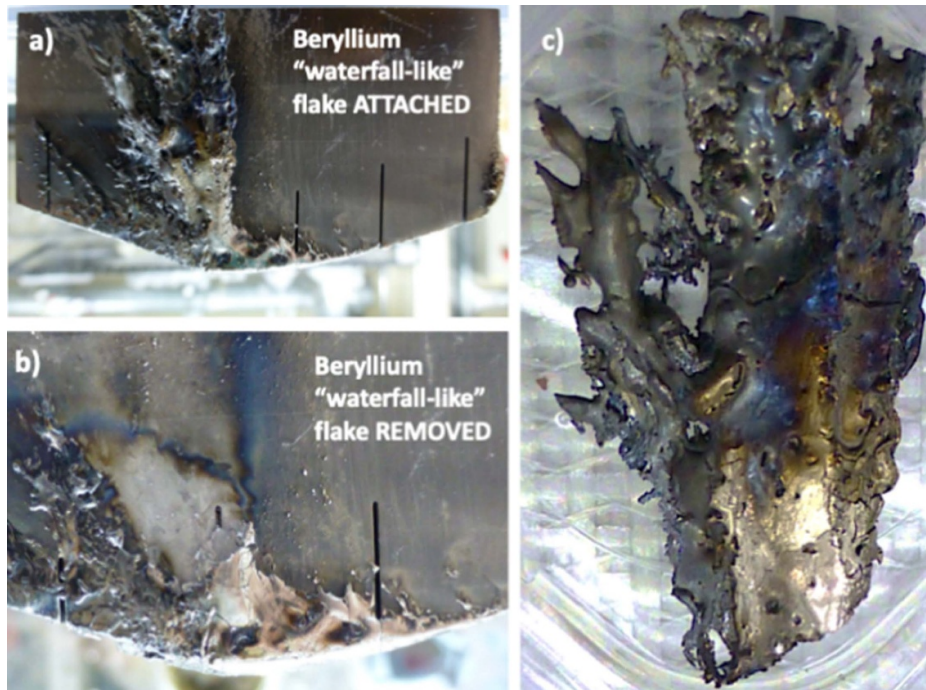


Figure 3. (a) Photograph of Be inverted ‘waterfall’ structure at the end of DP8; (b) after the Be flake was removed—with evidence that melted and solidified Be is still attached on the main tile, along with multiple droplets in different shapes and sizes; (c) full view of the Be ‘waterfall’.

As reported in [2] and described in section 2 the low field side tile of each of the 64 beams of upper limiters is characterized by the presence of an inverted Be ‘waterfall’ formation as depicted in figures 3(a)–(c). This structure is formed when the molten layer travels upwards, defying gravity in the poloidal direction from the high field side (inner wall) towards the low field side (outer wall), which is clearly attributed to melted material migration and re-solidification primarily due to the electromagnetic forces acting on the melt layer during a typical plasma disruption. The effect was earlier found and explained for molten tungsten in TEXTOR [3].

These structures were created primarily during the second operation campaign between 2013–2014 which was dedicated to high power scenarios with energy confinement optimization and ITER-relevant studies such as disruption mitigation by massive gas injection (MGI) [10]. Using a precision balance, the mass of the Be ‘waterfall’ structure was determined to 0.66 grams. Extrapolating to all 64 UDP beams, a total mass of 42 g was partially removed from the DPs, the value being of the same order of magnitude as the mass reported in [2]. The main point is that the $\mathbf{j} \times \mathbf{B}$ forces responsible for the Be molten layer movement across the DP tiles in poloidal direction was capable of mass dislocation in the range of 42 g for the entire JET vessel. Figure 3 along with the Be flake mass determination highlights again that Be melting, and layer movement is the main mechanism through which Be was lost from the UDPs.

A DP2 tile was removed after each experimental campaign and replaced with a new tile before the start of the next campaign, so that the accurate mass loss quantification from the tile could be performed [2]. The damage was not as obvious as that

for the tile neighbouring it, namely DP1 and DP3, since DP2 was exposed only during a single campaign. However, the melt damage and crack formation on the DP2 tiles from both experimental campaigns (2011–2012 and 2013–2014) was documented in [11] and profiling measurements of each DP2 tile before and after (figure 4(a)) the campaign was performed. The study estimated $\sim 150\text{--}200\ \mu\text{m}$ of material thickness was removed from the top apex of the tile after the second campaign (figures 4(b) and (c)). Extrapolation for the entire tile indicates that around 0.035 g of Be was lost. Further extrapolation for all the UDP tiles across the 64 UDP beams in the JET vessel would account for $\sim 18.2\ \text{g}$ of Be loss—which can be considered as the minimum amount (lower limit) of Be material lost from the UDP. In comparison, the weighing exercise performed in [2] reported $\sim 1\ \text{g}$ of Be lost for the DP2 tile, with an estimation of 129 g from the entire UDP set-up. It is stressed that the minimum value of $\sim 18.2\ \text{g}$ estimated by profiling, considers measurements of only 2 mm in length in the toroidal direction on the top edge castellation (figure 4) of DP2 tile after the second operational campaign, while the damage to it was extrapolated for the entire UDPs. These methods are representative for the lower and upper estimations of mass loss in the UDP tiles due to high heat loads during unmitigated plasma disruptions based on the available data and extrapolation assumptions.

2.2. Be splashing on diagnostic mirrors, wall, and probes

High-resolution photographic documentation of the upper wall of JET has provided a clear evidence of splashed matter in the vicinity of the UDPs and mushroom limiters (ML), both

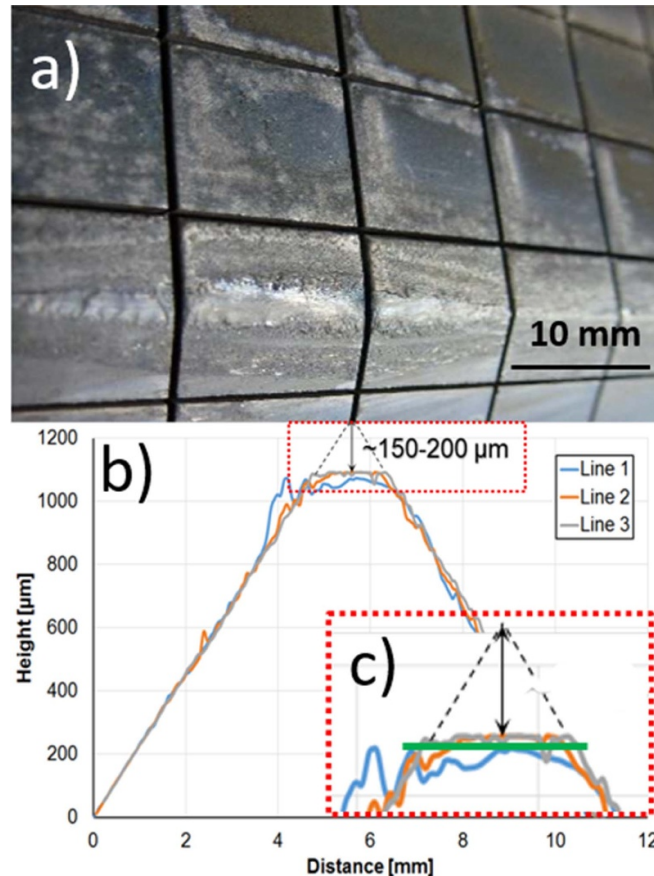


Figure 4. (a) Photograph showing close-up view of damage to the high field side DP2 tile, (b)–(c) estimation of material loss via profiling analysis in the range of $\sim 150\text{--}200\ \mu\text{m}$ in thickness.

made of solid Be. On this basis, the amount of Be deposited on the upper wall by splashing was assessed after two campaigns. In that region of JET it was not possible to place erosion-deposition probes such as those installed in the divertor and on the main chamber wall [12]. However, in addition to several blocks of UDP, one diagnostic component became available for ex-situ analyses: a gold-coated stainless-steel mirror from the lithium beam diagnostics (JET code KY6) for measurements of electron density profiles at the plasma edge under a wide variety of plasma shapes in JET [13]. The mirrors used in the first and second campaign were seriously damaged, as described in [14]. Therefore, although it was not possible to analyse Be splashes on the fixed elements of the wall, the KY6 diagnostic mirrors retrieved after two campaigns served as witness samples to enable the detection and analysis of Be in this region. Images in figures 5(a)–(d) show the general structure and details of the JET-ILW upper wall with respective elements indicated by numbers: the mirror (1), crane rail boss for fixing remote handling (RH) equipment (2) and beryllium PFCs: ML (3), UPD (4) and other, so-called sausage limiters (5). Areas with splashed Be are also marked (6). At the ends of the dump plates, one perceives molten beryllium layers (thick flakes) propagating upwards, as described earlier.

As documented by an infrared (IR) camera, disruptions at the top of JET affected very strongly DP8 tiles located above the outer divertor [2]. Therefore, besides the mirror surfaces,

the search for the presence of Be splashes was performed on outer poloidal limiters (OPL), and test mirror samples located at the outer wall (midplane position). Surface morphology of mirrors, dust monitors, and test mirrors was examined in detail by ion beam analysis and microscopy techniques: nuclear reaction analysis (NRA), Rutherford backscattering spectroscopy (RBS), optical microscopy (OM), scanning electron microscopy (SEM) and Be-sensitive energy dispersive x-ray spectroscopy (EDX). Focused ion beam cutting was used to obtain cross-sections of the splashes and to determine their thickness.

A number of SEM images in figure 6 show the mirror surface in the damaged area where arcing caused melting and melt layer motion. There are also Be splashes ranging in size ($200\text{--}400\ \mu\text{m}$) with diverse shape and structure displaying cracks or holes which may indicate boiling in the solidifying metal splash, e.g. figure 5(d). Clear images of the splashes in figure 6(a) and the strong Be $K\alpha$ line in the EDX spectra (figure 6(b)) suggest the absence of co-deposited species on the Be surface, thus indicating that the metal was ejected in the final stage of the second campaign when experiments with run-away electron generation were carried out.

Surface composition of the damaged and intact regions on the mirror obtained by RBS for Au and NRA for D and Be are in table 1. Considering the proximity of the mirror to the overheated UPDs, the Be content data could serve to assess

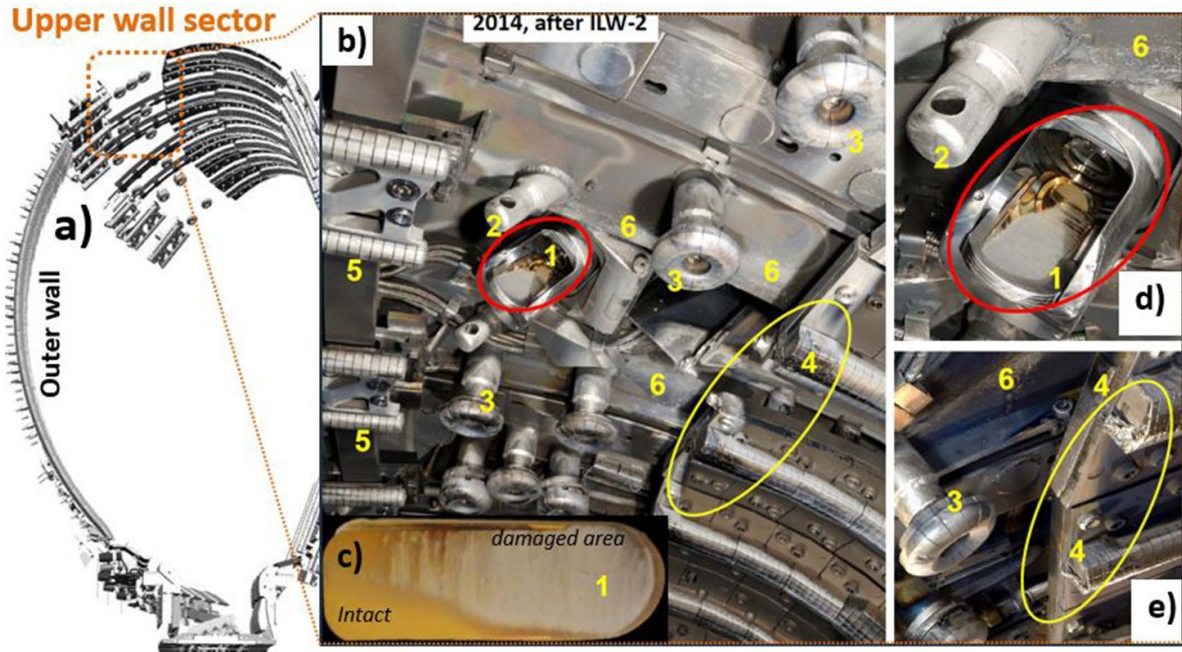


Figure 5. (a)–(e) View of the general location structure and details of the JET-ILW upper wall with respective elements indicated by numbers: the mirror (1), crane rail boss for fixing remote handling (RH) equipment (2) and beryllium PFCs: ML (3), UPD (4) and other, so-called sausage limiters (5). Areas with splashed Be are also marked (6).

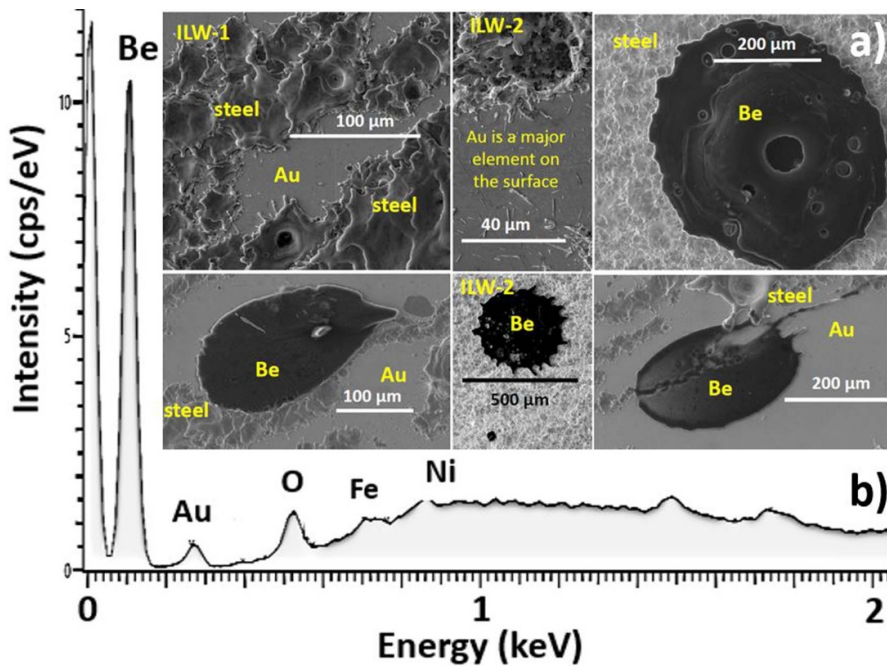


Figure 6. (a) SEM images of Be splashes on the upper wall on KY6 gold coated mirror and (b) corresponding EDX spectra.

Table 1. Deuterium, beryllium and gold concentrations in two areas on the Au-coated mirror after second ILW campaign. All concentrations are in 10^{15} cm^{-2} .

Area	D	Be	Au
Damaged	≤ 500	≤ 1000	1800
Intact	8	30	3700

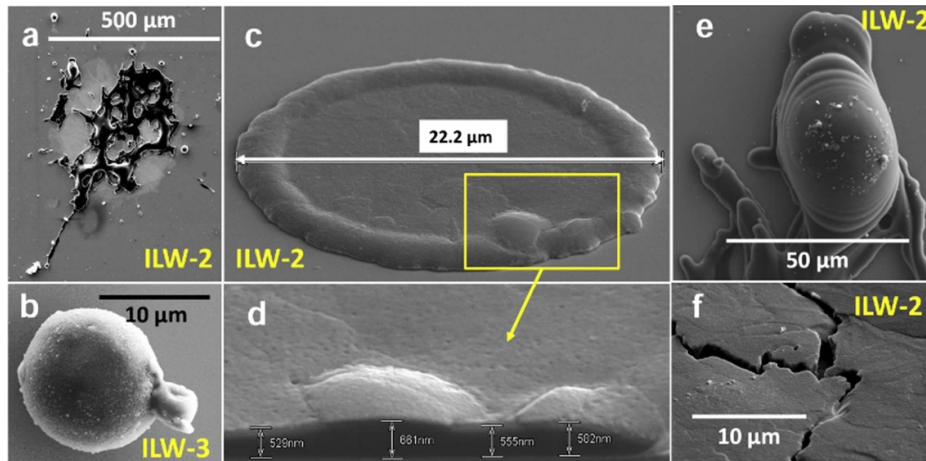


Figure 7. (a)–(f) Various forms of Be splashes found on the inner and outer wall dust monitors.

the quantitative share of Be evaporation to the total mass loss from the dump plates of 129 g in ILW-2 reported in [2]. With the maximum measured Be concentration of 1×10^{18} Be atoms cm^{-2} and assuming a uniform coverage of the entire JET wall (200 m^2) by Be evaporated from UDP one obtains 1×10^{24} atoms corresponding to 30 g of Be. This value is judged to be an overestimate; therefore, it can be considered as the upper limit. When taking into account the Be content ($3 \times 10^{16} \text{ cm}^{-2}$) on the undamaged mirror surface the lower limit is around 1 g. In summary, the data from the KY6 mirror (a witness plate for deposition on the upper JET wall) show that evaporation may be considered as a contributing but not the major mechanism for Be losses. Nonetheless, there is no clear evidence at this stage that the vaporised Be in the above assessment comes purely from the UDPs, and it could be an accumulation of both damage on the UDPs during unmitigated plasma disruptions and damage induced to other upper wall components like Be mushrooms and Be sausages tiles which were in the proximity of the mirrors.

2.3. Splashes on passive diagnostics and tile components

In-vessel high-resolution photographic survey carried out after each campaign has shown the presence of metal splashes on various wall components. It was not possible to carry out their elemental analysis, however, Be has been clearly identified as the main constituent of splashes on surfaces of mirror samples exposed at the outer wall midplane in JET within the first mirror test [14, 15]. Images in figures 7(a)–(f) show various forms of Be splashes and droplets on dust monitors from the inner and outer wall. Both their size and thickness vary within a broad range. In many cases these are flat circular (or only slightly elongated) objects with the thickness not exceeding several hundreds of nm, as shown in figures 7(c) and (d), and also described in [16, 17]. The presence of wrinkles resembling capillarity waves highlighted in figure 7(e) implies that the re-solidification of larger droplets ($50 \mu\text{m}$) did not occur instantaneously. Similar patterns have been previously identified during dust surveys in TEXTOR [18]. In some cases, the material was cracked, as in figure 7(f).

Microscopy examination of upper outer divertor Tiles 8, B and C has been carried out for the first time ever. The appearance of the tiles after ILW-3 is shown in figure 8(a), while other frames of that figure present a droplet and various shapes of beryllium splashes on the tungsten coating, figures 8(b)–(e) and an EDX spectrum with a clear Be feature, figure 8(f). Similar types of objects have also been found in samples collected on sticky pads from Tiles B and C. It should be noted that the splashes at the top of Tile 8 and protection Tiles B and C did not impact the plasma operations, as the outer strike point does not reach this region. As a consequence of minimal plasma interaction, Be analysis by EDX is possible because the splashes that collect there are not coated by co-deposits. Although there were many particles, they were quite small and covered a minimal area therefore the tile surfaces are still predominantly tungsten.

In summary, the presence of Be droplets, in a form of circular or elongated splashes ($1\text{--}500 \mu\text{m}$), has been detected in most samples from wall components. Their common feature is a firm adherence to surfaces in the location where they initially land. Such good adherence is a positive feature from the operation point of view and, it offers an explanation why only a small amount of loose Be dust particles is present in the dust sample collected by vacuum cleaning from the divertor [16]. However, the good adherence makes it difficult to assess precisely the erosion of limiters by melting and splashing as it is not possible to take multiple samples to quantify the mass of molten material spread around the vessel.

2.4. Be mass loss estimation due to Be ‘rain’ phenomena

One of the consequences of the unmitigated plasma disruptions was the Be ‘rain’ phenomenon happening from the top of the UDP right after some disruptions. Using the data [2] and starting from the 29 disruption triggering pulses which are considered mainly responsible for the UDP damage, a further analysis was performed to determine in which of these pulses the Be rain phenomenon occurred. The Be rain was identified using a near-infrared camera viewing a well-defined fraction of the torus (JET camera name KL7, viewing ~ 31 degrees

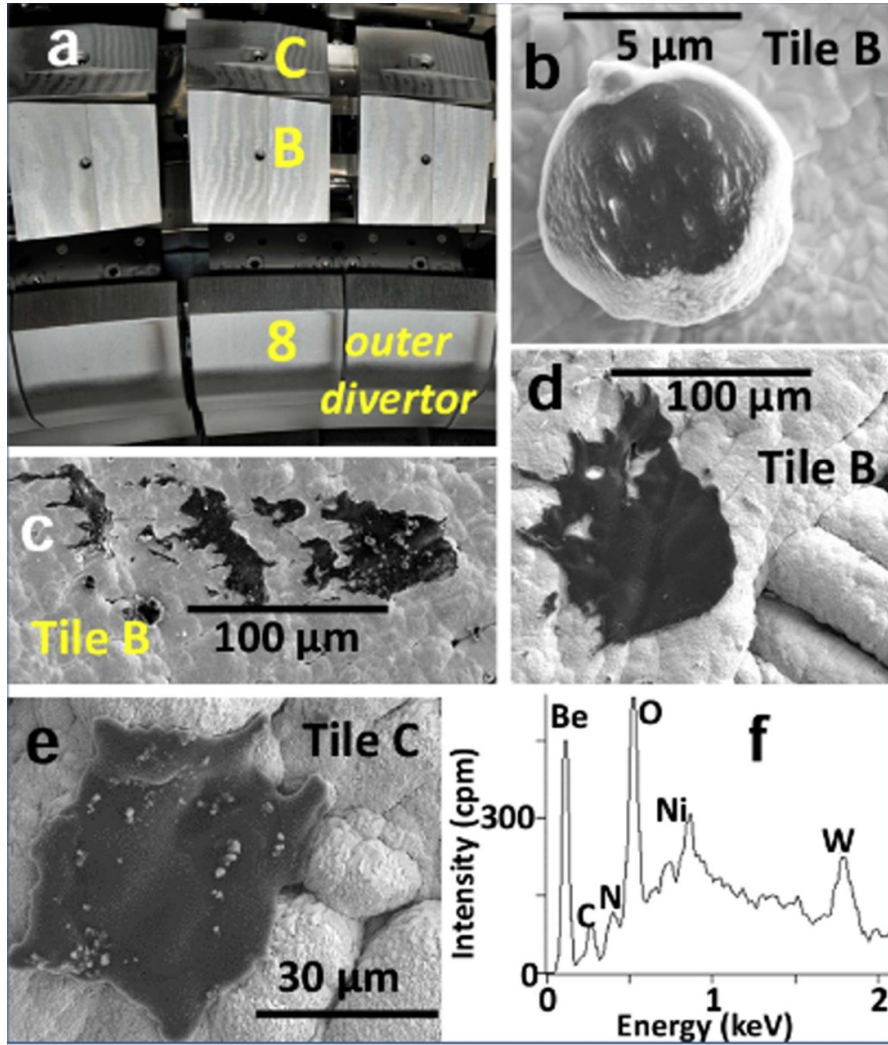


Figure 8. (a)–(e) Various forms of Be splashes found on the divertor tiles B and C and (f) the EDX spectrum with a clear Be feature.

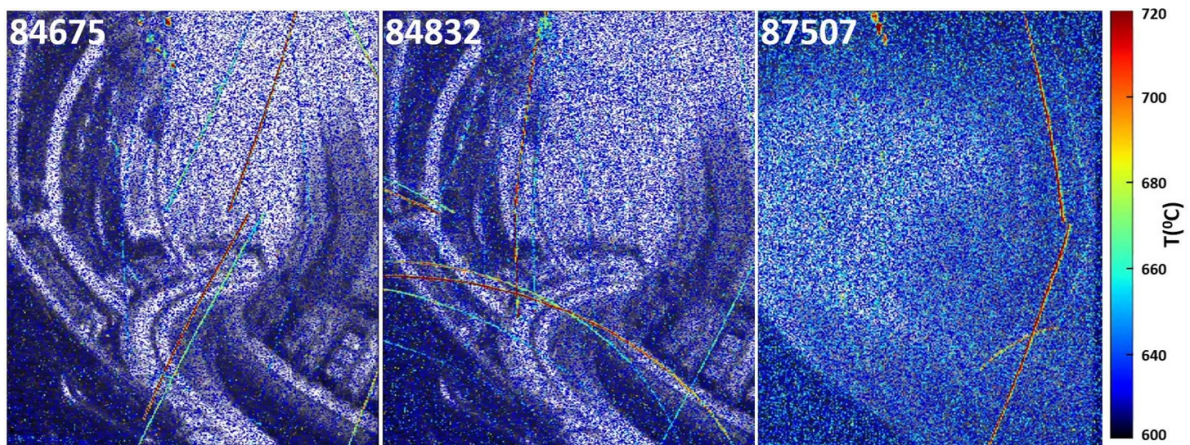


Figure 9. Post disruption Be ‘rain’ phenomena in three individual pulses as seen by the IR cameras.

toroidally). Figure 9 presents near-infrared photographic evidence of the thermal radiation emitted by heated Be droplets falling from the UDPs, captured with an exposure duration of 20 ms. Using another camera with a 600 μ s exposure time,

the velocity of the droplets was estimated to be in the range of 5–10 m s^{-1} . A summary of all pulses for which there is evidence of Be ‘rain’ is presented in table 2. In total nine pulses were identified and for each of these pulses, droplets visible

Table 2. Post disruption Be ‘rain’ phenomena.

Pulse no.	TOTAL no. of droplets	
	No. of counted droplets	Toroidal extrapolation of counted droplets
84 675	11	128
84 832	6	70
85 386	4	46
85 805	0	0
85 806	4	46
85 807	2	23
85 857	5	58
85 858	5	58
87 507	7	81
TOTAL	44	511

in the toroidal view were counted. Based on the pixel count per droplet and the camera’s resolution, it is estimated that the average diameter of the Be droplets observed falls between 3 and 4 mm. The camera used to estimate the droplet size has a depth of field of ~ 5 m, extending from the far wall around 6 m away to ~ 1 m in front of the camera. At the close limit of the camera depth of field, the pixel resolution is ~ 2 mm/pixel. From this perspective the pixel resolution is the limiting factor for the proper accountancy of small droplets. It is important to highlight that since the observed droplets are close to the pixel resolution limit, this could be a possible reason for the camera data being an over-estimate, hence the difference with the physical observation from droplets found in the divertor area presented in detail in section 2.3 of this work, where the size of Be splashes are less than 1 mm. As mentioned previously, the Be inverted ‘waterfall’ structure shown in figure 3, is present on all the 64 low field side tiles, namely DP8s, which suggests that at least for the main ejecting point of these falling droplets, the damage is evenly toroidally distributed. Therefore, the number of droplets observed by each IR camera in the 31° field view is extrapolated to 360° to give an upper limit for the number of droplets produced during the nine disruption events. A lower limit can be established by considering the asymmetry in a typical disruption as discussed in [2] wherein the lack of uniformity in toroidal melting distribution due to such events was highlighted. Based on these assumptions of symmetric and asymmetric melting from the unmitigated disruption events, the upper and lower count are summarised in table 2. From this data the mass loss from the DPs in the form of Be rain phenomena following nine unmitigated plasma disruptions events is estimated to be in the range 3 g–31 g where the lower figure represents the calculated Be mass for only the 44 droplets observed from the field of view of the cameras, while the upper value represents the mass extrapolation for the entire vessel. Note that, this amount of Be was not found when vacuuming the divertor after the campaigns. The reasons may include: (i) in their fall, the droplets end up in places where the vacuum cleaner

could not reach when collecting dust [16], i.e. in remote areas far from the heat of any plasma; (ii) droplets are well adhered to surfaces where they land, as noted in section 2.3, and therefore, cannot be vacuumed and, by this, do not contribute to the dust count; (iii) the vast majority of droplets that do end up on divertor surfaces are easily cleaned and evaporated with the following pulses, being transported to various regions of the vessel as co-deposits. There were very few cases of big droplets being found during the shutdown intervention [17], mainly because of the reasons given above, but one of those instances is shown in figure 10 where a Be droplet, following Be rain in pulse no. #84832 was found on Tile B of the outer divertor (figures 10(d) and (e)). A schematic including the position of the UDPs in relation to the position of this droplet is highlighted in figures 10(a)–(e). To guide the eye, the area where droplets could have fallen from the UDP into the outer divertor is highlighted in figure 10(a). The near IR image in figure 10(b) supports the statement that the large droplet depicted in figures 10(d) and (e) is a direct consequence of the disruption event in pulse no. #84832. The area of the droplet in figure 10(e) is ~ 55 mm². Nevertheless, one needs to take into consideration that the dimensions of this droplet may have suffered many changes following 3126 pulses in the second campaign, including cleaning pulses, which could have affected its overall shape and dimension. Based on the current limitations of in-vessel imaging, no estimation can be made of its actual thickness, nonetheless even the high-resolution image is sufficient evidence of the size of this droplet.

3. Runaway electron damage on beryllium plasma facing components (ii)

The generation of highly energetic RE originating from unmitigated plasma disruptions poses serious threats to PFC in fusion devices like ITER, DEMO. In the ITER case, RE can be accelerated to energies in the MeV range. Due to their

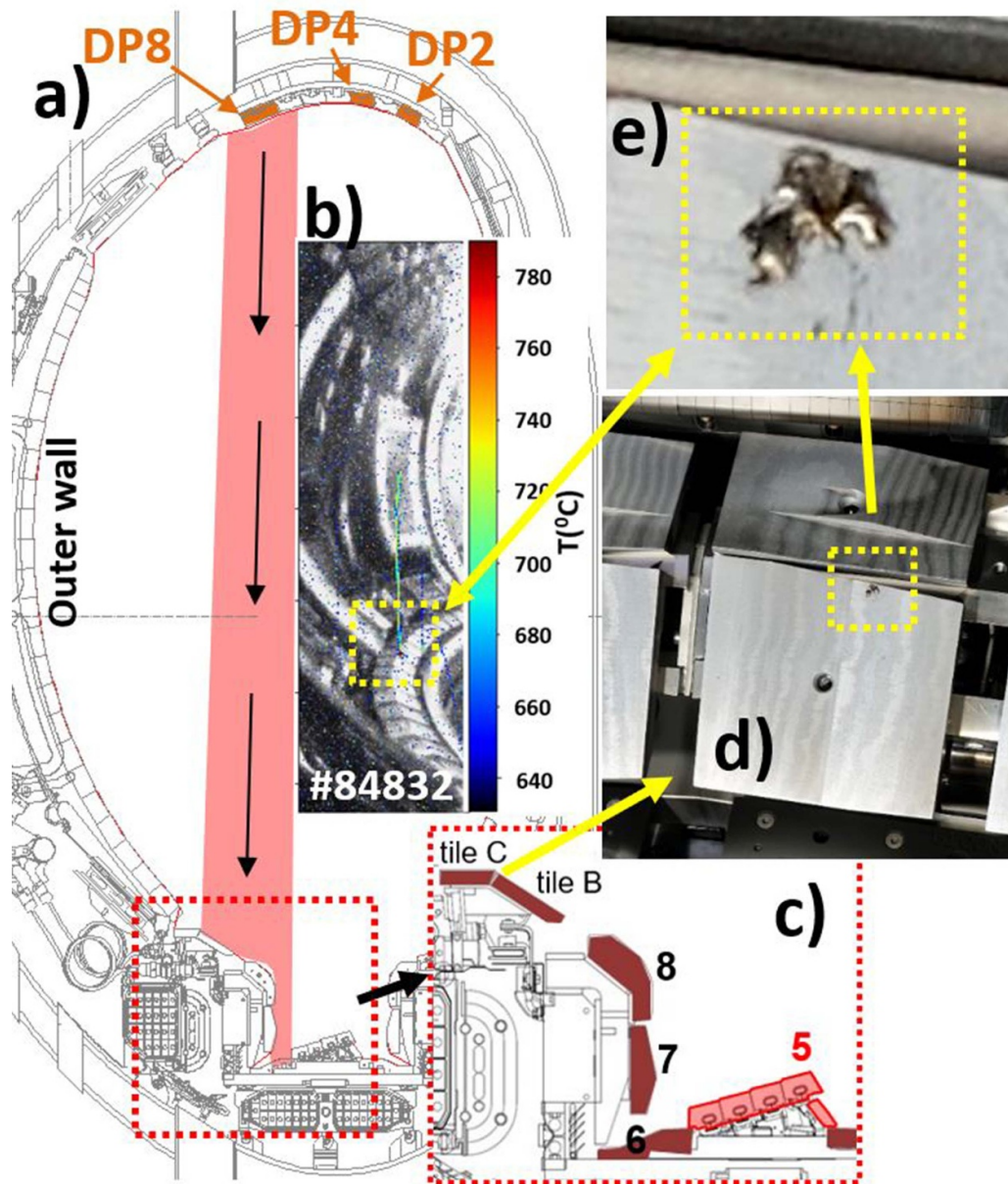


Figure 10. (a) JET cross-section with projection from the UDP to the possible location of Be ‘rain’ droplets once the magnetic field is off after a disruption; (b) near IR image post pulse no. #84832 highlighting the large droplet in the outer divertor; (c) a cross-section of the divertor with an indication to Tile B (d) and (e) a close-up view of the droplet found after the second campaign.

unpredictable nature and the lack of a fully reliable mitigation system to suppress their effects on fusion reactor behaviour, and ultimately to the components that can be affected by them, a series of studies were performed in different tokamak environments [19–21]. The focus of this section is to highlight the damage that was produced on the Be components in the JET reactor following such events. It is worth mentioning that since the installation of the metallic wall in JET in 2011, REs have not been produced during typical discharges, though they were common in the JET with carbon walls [22]. During the second campaign (2013–2014), there were dedicated experiments for studying such events in JET. REs were intentionally induced using MGI with Argon (Ar) [4] to trigger

the conditions for disruptions and ultimately to produce REs. A small number of sessions dedicated to RE significantly limited the damage caused by these events thus allowing for an accurate identification of the affected components.

3.1. Visual observation via imaging, OM and 3D profiling

The first signs of the effect of REs on the PFC were reported in [4, 6]. Using the In-Vessel Inspection System (IVIS) cameras in JET following dedicated RE experiments, it was confirmed that damage occurred to the IWGL tiles. Further high-resolution imaging inspections, carried out after the campaign in 2014, reinforced and clarified the results regarding

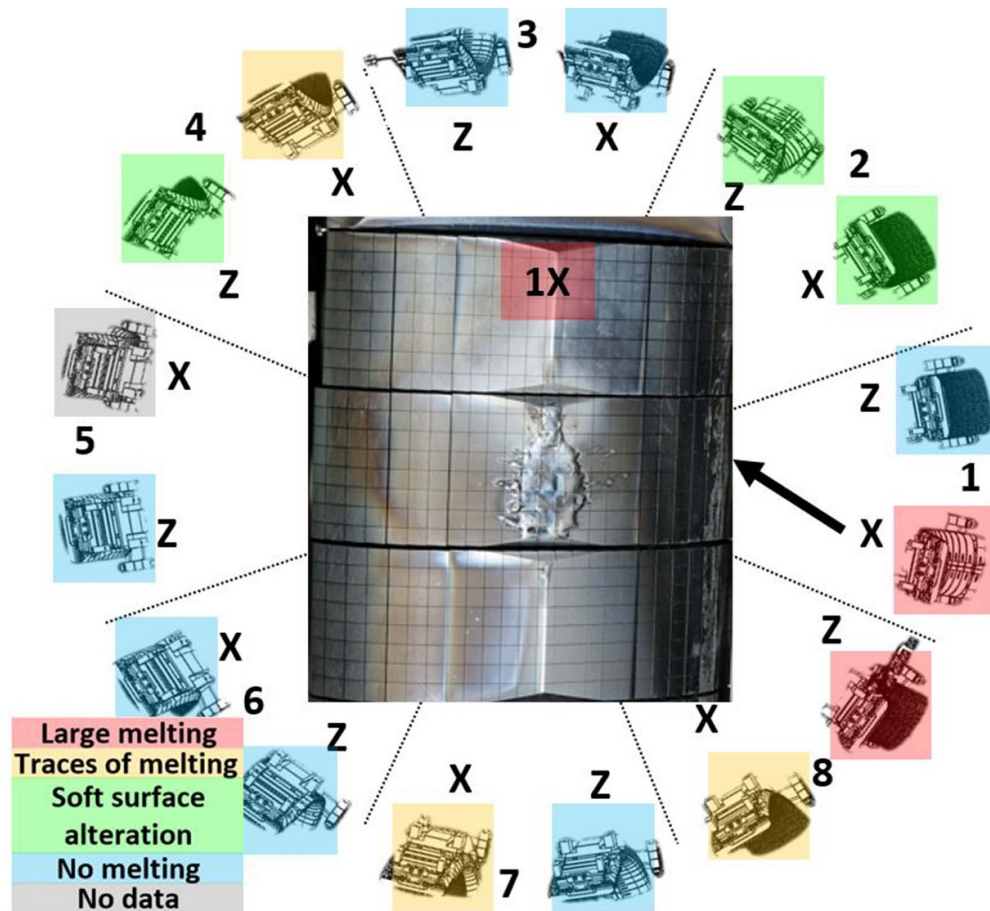


Figure 11. Toroidal distribution of the IWGL beams in JET reactor, with a photograph in the centre from the 1X beam showing localised damage from runaway electrons. The toroidally asymmetric damage due to the REs is highlighted by the colour map.

the damage to the inner wall [4]. A characteristic feature of the REs was the non-uniform behaviour of such events having a significant and highly localised impact on wall components which was not toroidally distributed around the JET machine. A similar behaviour was reported in [2], where the damage from the unmitigated plasma disruption to the UDP was seen not to be fully symmetrical. In the case of REs, it is more obvious that these events were locally generated, hence they affected smaller regions at the inner wall. Although every Be limiter on the inner wall was positioned in accordance with the specified and assembly tolerances of ~ 1 mm, one of the reasons for this lack of toroidal symmetry could be due the geometry and tile arrangements in JET, correlated with the actual location of the MGI injections required for triggering the events. The second reason is the very complex nature of such events [4]. During the 2017 intervention, when several PFCs were replaced with new ones for the upcoming experimental campaigns, one of the RE damaged tiles was removed. In the following, morphological and structural analysis of this tile is presented. The first damage assessment was carried out during the remote post-experimental inspection. Figure 11 shows the toroidal distribution of the IWGL Be beams in JET and summarises the location and severity of damage to the tiles. As previously reported, this demonstrates that the toroidal distribution of the damaged tiles due to the REs is not

uniform. There are only two heavily affected tiles, namely on the 1X and 1Z inner limiter beams, while the rest have either no visible damage or only slight traces of it. The lack of uniformly distributed damage is also observed in poloidal direction, since the only affected tile from the 1X beam is the one shown in the centre of the image. A closer look to the damage feature was possible once the damage tile was removed during the 2017 intervention. In the following, morphological and structural analysis of this tile is presented.

Figure 12(a) shows a high-resolution image of the affected tile once retrieved from the torus. To assess the magnitude of the damage, a 3D profiling measurement was conducted using a AL147 FARO Edge with AL148 laser line probe. These results were directly used for damage modelling purposes. Figure 12(b) is a colour map of the damaged tile surface, revealing the extent and distribution of the erosion induced by the REs. The generated profiling image in figure 12(b) is based on a comparison with a reference model of an undamaged tile. The colours correspond to different levels of deviation from the reference. The colour 'green' depicts no change as compared to the reference, meaning that the tile surface was unaffected. The 'blue' colour represents the points that were between 1–2 mm lower than the reference, highlighting damage in the form of 'pools' on the tile surface. These pools are the result of Be melting and evaporation due to extreme

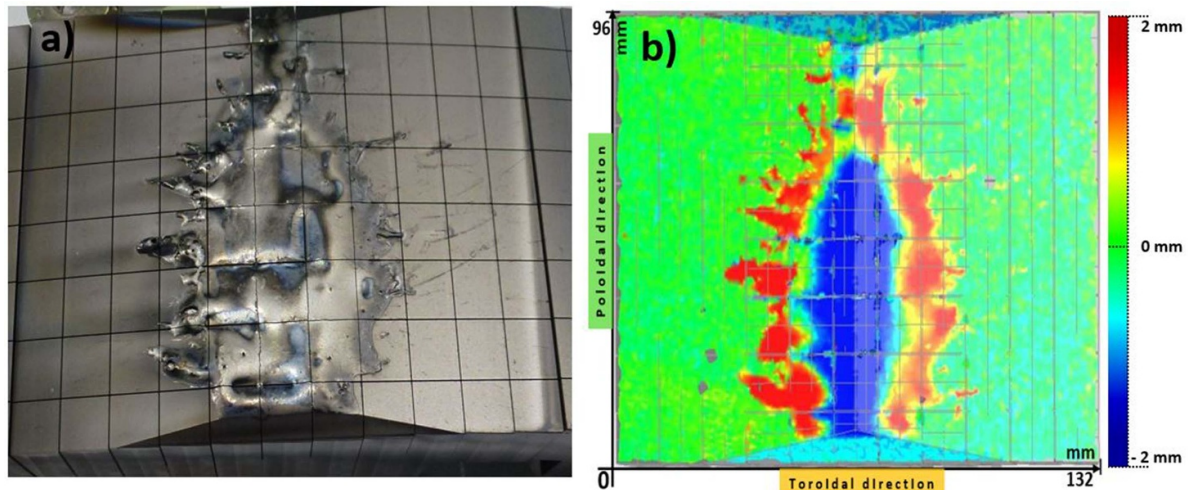


Figure 12. (a) Photograph of RE damaged tile and (b) reconstructed damaged surface via tile 3D profiling.

heat induced by the runaways. The ‘red’ colour corresponds to points that were 1–2 mm above the reference revealing damage in the form of ‘hills’ on the tile surface. These protrusions to the tile surface are most likely the consequence of material displacements and re-solidification of Be after the tile was hit by the REs. The analysis shows that the RE impact caused considerable damage, but was focused on one tile only thus confirming previous statements that the REs impact was very localized without any major effect on the surrounding PFC.

For a better assessment of the depth damage generated by the REs, the tile was cut in four quarters (figure 13(a)). Optical micrographs in figure 13(b) show the extent of the damage in the poloidal direction across four individual castellations. The images provide evidence of molten material bridging gaps between adjacent castellations, a similar behaviour as seen in [2]. However, no accumulation of molten material penetrating into the castellation grooves is observed. In line with the melt propagation mechanisms discussed in [6], this result is the first experimental evidence showing clearly the distinction between melting effect from REs and unmitigated disruptions. For the unmitigated disruptions, $\mathbf{j} \times \mathbf{B}$ forces arising from thermal electron emission in a magnetic field moved material in the poloidal direction filling partially the gaps. Whereas for REs, although there is a significant current, melting is deeper into the surface with no thermionic emission compensation current being generated to drive $\mathbf{j} \times \mathbf{B}$ forces and move the melt layer. In addition, any strong current flow resulting from the REs (disregarding the magnetic field’s influence on the electrons scattered within the material) is predominantly parallel to the toroidal field, thus not contributing to the $\mathbf{j} \times \mathbf{B}$ drive [6]. Therefore, the castellation gaps are not filled by RE melting, as shown here. Measurements revealed a difference in height of material displacement of 1.2 mm for the measured section (figure 13(c)),

which was consistent with the 3D profiling results. Using the DINA-SMITER-MEMOS-U [23] together with GEANT4 toolkit, modelling of this damage was performed [24, 25]. The modelling revealed a good agreement with the ex-situ measurements for reasonable assumptions for the incident RE parameters (REs energy distribution of 12.9 MeV obtained from gamma ray spectrometry and 6 ms pulse duration) guided by the experiment [4, 6]. The material boiling patterns, volume and depth damage were consistent with the experimental findings.

3.2. Morphological and structural analysis

To assess the crystalline nature and the chemical composition of the melted region on the Be limiter due to the REs impact, *x-ray diffraction* was performed. A parallel slit collimator of 0.5° with a 1 mm slit opening was placed in front of the sample to limit the incident x-ray beam divergence and to expose only the desired regions (S0–S4) as highlighted in figure 14(a). The corresponding diffraction patterns for each strip S0–S4 are shown in figure 14(b), with an offset for a better visualization. The main outcome of this investigation highlights the presence of two distinct crystalline phases: a dominant one corresponding to the metallic Be (hexagonal close-packed structure) with preferential crystalline growth on the 101-diffraction plane, and a BeO phase observed to the left of the Be 101 peak by three additional peaks, centred at 38.5° , 41.2° and 44° respectively. Regions S2–S4 corresponding to an analysis depth of 2–5 mm show almost identical diffraction patterns, with a similar symmetry to that of a typical Be polycrystalline structure. This characteristic is furthered documented by the in-depth comparison of the Be 101 peak intensities shown in figure 14(c) indicating that the RE events do not result in changes to the crystalline structure below the 2 mm threshold in the examined Be castellation. However, for the S0

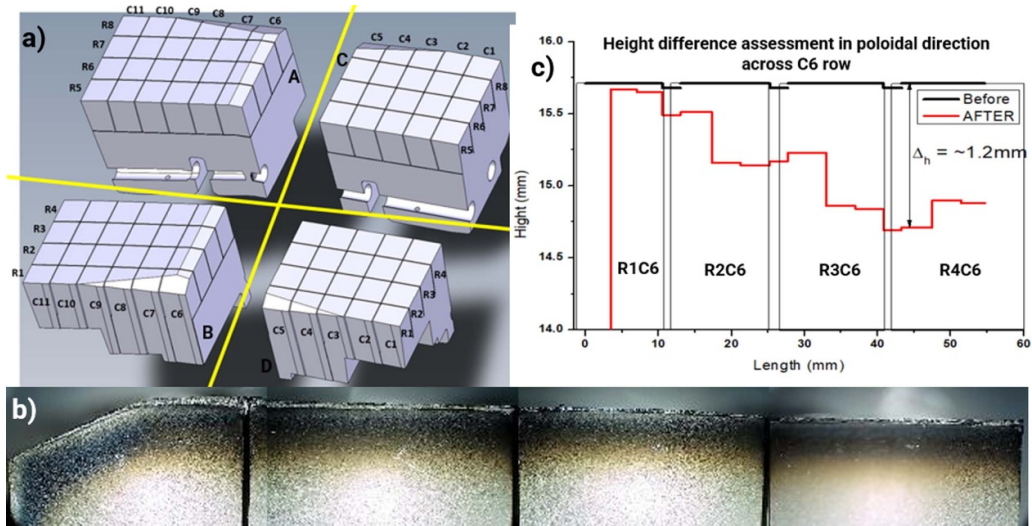


Figure 13. (a) View of split tile with (b) optical microscopy in the poloidal direction showing close-up view of melting at the surface and (c) height difference measured in the poloidal direction.

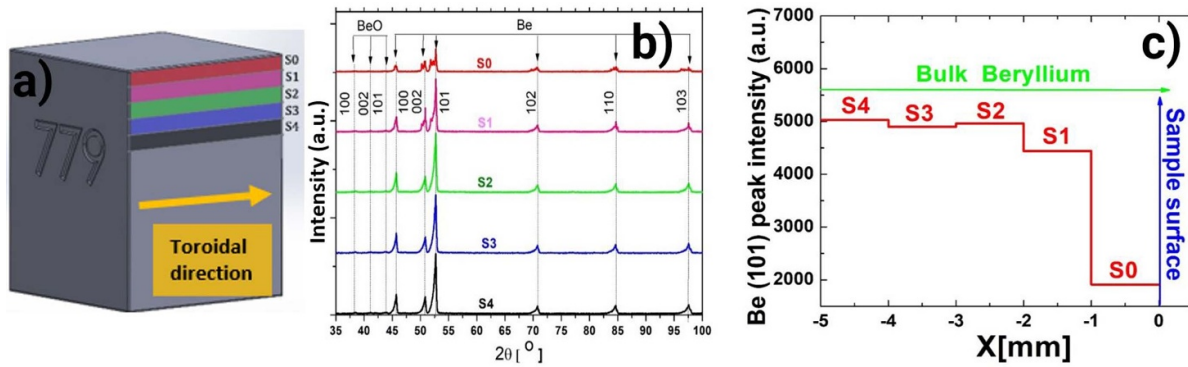


Figure 14. (a) Representation of x-ray measurement patterns; (b) diffraction patterns for all analysed regions; (c) comparison of Be 101 relative intensity.

surface region, the extinction of the Be 101 scattering centres by $\sim 60\%$ compared with the S2–S4 areas and a peak broadening suggests a transition to an amorphous state of Be near the surface. The overall measurement was performed using a Rigaku Ultima IV diffractometer using a Cu-K α radiation source (0.154 nm) and a D/teX Ultra 1D silicon strip detector with a graphite monochromator. Measurements were done in the θ – 2θ geometry ranging from 33° to 100° with a step of 0.05° .

Electron backscattering diffraction (EBSD) combined with Scanning Electron Microscopy (SEM) were performed to visualize the topography and crystallographic structure of the RE damaged region. Figure 15(a) depicts the secondary electron image of the analysed castellation. The right side is the plasma facing surface affected by the REs, while figure 15(b) highlights the surface normal-projected inverse pole figure orientation map of the near-surface region of the plasma-affected Be. The results demonstrate that material melted and then re-solidified in the 330 μm thick near surface region. The re-solidified phase has columnar grain structure

with a long grains perpendicular to the exposed surface. The lengths of these grains often equal to the depth of the melted-resolidified layer. In the area deeper than the melted layer, the base material has uniaxial grains (avg. diameter $< 10 \mu\text{m}$) typically observed in vacuum hot-pressed beryllium grades [26]. Many non-cubic metals including beryllium have strong anisotropy of thermal expansion, therefore can be deformed by heating and cooling. During cooling of a polycrystalline Be, its anisotropy leads to development of a compressive internal stress along the $\langle c \rangle$ axis of grains and a tensile stress along the $\langle a \rangle$ axis of grains. At high temperatures these intergranular stresses may relax by material deformation introducing dislocations and micro-twins and also creation of microvoids. The micro-twins and degradation in the EBSD pattern quality, which are a sign of a higher dislocation density have been detected in the resolidified grains. Microvoids were observed both in as received and re-solidified materials. However, visually, more voids were observed in the melted areas with occasional lineal agglomeration around grain boundaries.

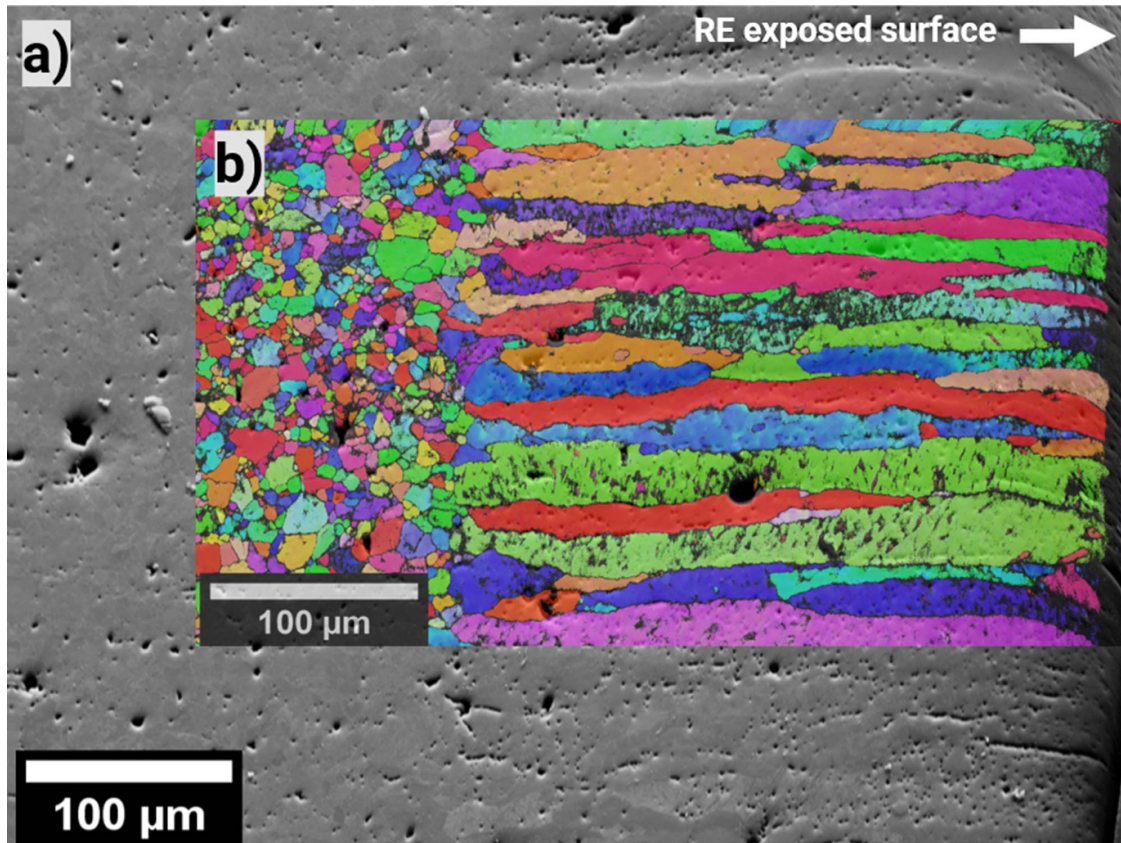


Figure 15. (a) Secondary electron image of the REs damaged region with a focus on the (b) inverse pole figure orientation map.

4. Conclusions

A major contribution of this work to fusion-related material studies is a detailed analysis and quantification of effects caused by unmitigated plasma disruptions and REs events on the Be PFC in JET tokamak. The results have provided new evidence of Be layer motion and migration during high heat loads, and intense electromagnetic forces. Based on the tile profiling and quantification of the Be ‘rain’ phenomena, a comprehensive set of data on Be mass loss was estimated. The values represent most probably the lower limit of Be mass loss because of restrictions in the physical access to in-vessel materials thus having an impact on the extrapolations. Evidence for evaporation as a source of mass loss is minimal. REs production represents one of the consequences of unmitigated plasma disruptions, with massive damaging impact on PFC. High resolution surveying, 3D-profiling and microscopy techniques have provide data serving as an input to benchmark codes for modelling of RE events. As a consequence, modelling results were in very good agreement with the physical observations in terms of depths, areas, and direction of melt damage [24, 25]. Crystallographic analysis of the RE affected regions revealed a change in the crystalline structure surrounding the affected region, with elongated grain formation and

induced micro-voids. The work has yielded the most comprehensive data on Be melting in a fusion environment and, by this, provided background information for future fusion studies of JET materials after the full D-T campaigns in JET, and in other fusion experiments if Be components would be used.

Acknowledgments

This work has been carried out within the framework of the EUROfusion Consortium, funded by the European Union via the Euratom Research and Training Programme (Grant Agreement No 101052200—EUROfusion) and from the EPSRC [Grant Numbers EP/W006839/1]. Views and opinions expressed are however those of the author(s) only and do not necessarily reflect those of the European Union or the European Commission or the ITER Organization. Neither the European Union nor the European Commission can be held responsible for them.

The research used UKAEA’s Materials Research Facility, which has been funded by and is part of the UK’s National Nuclear User Facility and Henry Royce Institute for Advanced Materials.

ORCID iDs

I. Jepu  <https://orcid.org/0000-0001-8567-3228>
 A. Widdowson  <https://orcid.org/0000-0002-6805-8853>
 S. Brezinsek  <https://orcid.org/0000-0002-7213-3326>
 M. Rubel  <https://orcid.org/0000-0001-9901-6296>
 G. Pintsuk  <https://orcid.org/0000-0001-5552-5427>
 E. Fortuna-Zalesna  <https://orcid.org/0000-0002-1090-1641>
 C. Porosnicu  <https://orcid.org/0000-0003-0561-0644>
 P. Dinca  <https://orcid.org/0000-0003-4383-9941>
 O. Pompilian  <https://orcid.org/0000-0001-6031-2880>
 B. Butoi  <https://orcid.org/0000-0002-2780-1751>
 S. G. Moga  <https://orcid.org/0000-0001-9620-4283>
 S. Silburn  <https://orcid.org/0000-0002-3111-5113>
 S. Kuksenko  <https://orcid.org/0000-0001-7668-112X>
 E. Alves  <https://orcid.org/0000-0003-0633-8937>
 N. Catarino  <https://orcid.org/0000-0003-3879-1533>
 R.A. Pitts  <https://orcid.org/0000-0001-9455-2698>
 L. Chen  <https://orcid.org/0000-0003-4233-5936>
 S. Ratynskaia  <https://orcid.org/0000-0002-6712-3625>

References

- [1] Pitts R., Buttery R. and Pinches S. 2006 *Phys. World* **19** 20–26
- [2] Jepu I. et al 2019 *Nucl. Fusion* **59** 086009
- [3] Sergienko G. et al 2007 *Phys. Scr.* **T128** 81–86
- [4] Reux C. et al 2015 *Nucl. Fusion* **55** 093013
- [5] Matthews G.F. et al 2011 *Phys. Scr.* **T148** 014001
- [6] Matthews G.F. et al 2016 *Phys. Scr.* **T167** 014070
- [7] Sergienko G. et al 2014 *Phys. Scr.* **T159** 014041
- [8] Ratynskaia S., Thorén E., Tolia P., Pitts R.A., Krieger K., Vignitchouk L. and Iglesias D. 2020 *Nucl. Fusion* **60** 104001
- [9] Vignitchouk L., Ratynskaia S., Pitts R.A., Lehnen M. and Contributors J. 2022 *Nucl. Fusion* **62** 036016
- [10] Lehnen M. et al 2011 *Nucl. Fusion* **51** 123010
- [11] Pintsuk G., Brezinsek S., Coenen J.W., Huber A., Rubel M. and Widdowson A. 2020 *Phys. Scr.* **T171** 014042
- [12] Rubel M. et al 2013 *J. Nucl. Mater.* **438** S1204
- [13] Brix M. et al 2010 *Rev. Sci. Instrum.* **81** 10D733
- [14] Garcia-Carrasco A., Petersson P., Rubel M., Widdowson A., Fortuna-Zalesna E., Jachmich S., Brix M. and Marot L. 2017 *Nucl. Mater. Energy* **12** 506
- [15] Moon S. et al 2019 *Nucl. Mater. Energy* **19** 59
- [16] Rubel M. et al 2018 *Fusion Eng. Des.* **136** 579
- [17] Fortuna-Zalesna E., Grzonka J., Moon S., Rubel M., Petersson P. and Widdowson A. 2017 *Phys. Scr.* **T170** 014038
- [18] Ivanova D., Rubel M., Philipps V., Freisinger M., Huang Z., Penkalla H., Schweer B., Sergienko G., Sundelin P. and Wessel E. 2009 *Phys. Scr.* **T138** 014025
- [19] Lehnen M., Abdullaev S.S., Arnoux G., Bozhenkov S.A., Jakubowski M.W., Jaspers R., Plyusnin V.V., Riccardo V. and Samm U. 2009 *Nucl. Mater.* **390–391** 740–6
- [20] Saint-Laurent F. et al 2011 *Proc. 38th EPS Conf. on Plasma Physics (Strasbourg, France, 27 June–1 July 2011)* vol 33E p O3.118 (available at: <https://info.fusion.ciemat.es/OCS/EPS2011PAP/pdf/O3.118.pdf>)
- [21] Hollmann E.M. et al 2013 *Nucl. Fusion* **53** 083004
- [22] Gill R.D. et al 2002 *Nucl. Fusion* **42** 1039
- [23] Coburn J. et al 2021 *Nucl. Mater. Energy* **28** 101016
- [24] Chen L. et al private communication
- [25] Chen L. et al 2021 *5th Asia Pacific Conf. on Plasma Physics (26 September–1 October)* (available at: <https://www.aappsdp.org/DPP2021/>)
- [26] Kuksenko V., Roberts S. and Tarleton E. 2019 *Int. J. Plast.* **116** 62–80